J. Fluid Mech. (1998), *vol.* 355, *pp.* 285–315. Printed in the United Kingdom

Stationary travelling cross-flow mode interactions on a rotating disk

By T. C. CORKE AND K. F. KNASIAK

Fluid Dynamics Research Center, Mechanical and Aerospace Engineering Department, Illinois Institute of Technology, Chicago, IL 60616, USA

(Received 26 March 1997 and in revised form 11 September 1997)

This work involves the study of the development of Type 1 stationary and travelling cross-flow modes in the three-dimensional boundary layer over a rotating disk. In order to control the characteristics of the stationary modes, we utilized organized patterns of roughness which were applied to the disk surface. These consisted of ink dots which were equally spaced in the azimuthal direction at a fixed radius in order to enhance particular azimuthal wavenumbers. Logarithmic spiral patterns of dots were also used to enhance azimuthal wave angles. Velocity fluctuation time series were decomposed into the components corresponding to the stationary and travelling modes using the instantaneous disk position as a reference. Their development was documented through the linear and nonlinear stages leading to turbulence. The linear stage agreed well with linear stability predictions for both modes. In the nonlinear stage we documented a triad coupling between pairs of travelling modes and a stationary mode. The strongest of these was a difference interaction which lead to the growth of a low-azimuthal-number, stationary mode. This mode had the largest amplitude and appeared to dominate transition. In retrospect, we can observe the signs of this mechanism in past flow visualization (Kobayashi, Kohama & Takamadate 1980), and it can account for the 'jagged' front normally associated with cross-flow-dominated transition on swept wings.

1. Background

The boundary layer flow over a rotating disk in a quiescent fluid has frequently been used as a canonical three-dimensional flow which exemplifies the cross-flow instability. In this flow, the instability appears as outward-spiralling waves. These were first detected experimentally in the hot-wire measurements of Smith (1946). The theoretical analysis accompanying experimental results followed later in the classic paper by Gregory, Stuart & Walker (1955). In that they surmised a number of key elements about this instability such as the role small surface roughness could have in fixing the locations of stationary modes, and the expected existence of travelling modes which could not be detected in their surface flow visualization.

Even though linear theory predicts the travelling modes to be more amplified, a majority of the experiments have focused on stationary cross-flow modes. The reasons for this are two-fold. The first is that many of the studies have been based on flow visualization (Gregory *et al.* 1955; Fedorov *et al.* 1976; Kobayashi, Kohama & Takamadate 1980; Kohama 1984) which tends to emphasize stationary components. The second is the sensitivity of this instability to surface roughness which can bias the larger-amplitude modes towards the stationary type. For example, Wilkinson &

Malik (1985) observed that stationary modes originated from small randomly placed dust particles on the surface of a 'clean' disk. This prompted them to study the effect of a single isolated surface roughness. From this they observed the growth of wave packets which rapidly spread around the disk to eventually fill the entire circumference. Some very beautiful flow visualization of the spiral wave development with a single roughness element in the same setup was done by Blanchard (1992). Jarre, Le Gal & Chauve (1996) investigated nonlinear effects produced by a single roughness piece with a height which was equal to the boundary layer thickness. They observed the spreading of the generated wave packet, and found that the propagation angle of the forced waves was different from the natural angle of propagation.

From a theoretical point of view, the rotating disk flow is attractive because the mean flow has an exact solution. Malik, Wilkinson & Orszag (1981) developed a linear stability analysis of this basic flow which included Coriolis forces and streamline curvature. The linear theory was used to predict the location of transition to turbulence by an e^N extrapolation, which they compared to previous experiments, such as those cited above. Other notable numerical studies of the linear instability of this flow include Mack (1985), Malik (1986), and Faller (1991). In addition to these, Spalart (1991) performed a direct numerical simulation for a variety of roughness conditions, including those of Wilkinson & Malik (1985). A general review of the stability of three-dimensional boundary layers including the rotating disk was given by Reed & Saric (1989).

A larger body of experimental work on the nature of the cross-flow instability exists for swept wings. These include the work by by groups at DLR (Müller & Bippes 1988; Bippes 1991), at Arizona State University (Dagenhart *et al.* 1989; Kohama, Saric & Hoos 1991; Radeztsky *et al.* 1993) and at ONERA/CERT (Arnal & Juillen 1987). The experiment of Müller & Bippes (1988) is somewhat singular because it was one of the few to show both stationary and travelling cross-flow modes. In this case they did not observe the generation of a high-frequency secondary instability mode leading to transition, which has been generally attributed to the breakdown of cross-flow vortices on disks (Kohama 1984, 1987) and on a swept cylinder (Poll 1985). However in the stationary-mode-dominated swept wing experiment of Kohama *et al.* (1991), a high-frequency secondary instability was observed just prior to transition.

The apparent conflict in the two experiments can be reconciled by the noted differences in the amplitude level of the travelling modes. Müller & Bippes (1988) studied the effect of the free-stream turbulence level on the amplitude of the stationary and travelling modes. They found that at low levels ($\leqslant 0.05\%$), which are comparable to the ASU experiments, the transition was dominated by stationary modes. However at higher levels (0.15% to 0.3%), the travelling modes became more dominant. In these cases, although the growth of the stationary mode was less, transition occurred earlier. From this they concluded that the travelling modes were more important to transition.

These results, for which stationary and travelling cross-flow modes exist at comparable levels, open the possibility of a nonlinear interaction between them. Lekoudis (1979) was one of the first to consider the possibility of a triad-type interaction between travelling cross-flow waves in the three-dimensional boundary layer on a swept wing. For the same flow, Malik, Li & Chang (1994) used a nonlinear model to study the interaction between travelling and stationary cross-flow modes. They considered only 'tuned' resonance cases with a pair of travelling modes with the same frequency and equal and opposite spanwise wavenumbers. They observed that the modes could interact and that the final stage was dependent on their relative initial amplitudes. For

example when the initial amplitudes of the travelling and the stationary modes were the same, the travelling modes, owing to their larger growth rates, would dominate most of the flow development. Further confirmation has recently come from DNS computations for a swept-wing boundary layer by Müller, Bestek and Fasel (1995). In this case they used different artificial initial conditions to investigate the nonlinear interaction between a stationary and a travelling cross-flow mode. These were found to lead to a number of cases in which a triad resonance could be verified. At present there has been no experimental confirmation.

In the present work we use the flow over a rotating disk as a means to study mechanisms for transition to turbulence originating from the cross-flow instability. The emphasis is on documenting the development of travelling modes, and determining their role in the transition process with an eye towards nonlinear interactions with stationary modes. In an effort to better control the initial conditions, owing to the sensitivity of this instability to surface roughness, we use an earlier technique (Corke & Knasiak 1994) and apply an array of roughness 'dots' to the surface of the disk. The azimuthal number of dots would be chosen based on the azimuthal wavenumber most likely to occur naturally (be most amplified based on linear theory). It was intended that the scale (height and diameter) of the dots should be sufficient to put energy into a narrow band of modes, but not be so large as to change the basic flow. With different dot conditions, we document changes in the unsteady flow and attempt to isolate the respective contributions to stationary and nonstationary components which lead to transition to turbulence.

2. Experimental setup and procedure

2.1. *Setup*

The rotating disk facility consists of a polished aluminium disk mounted on an air bearing with an integrated d.c.-motor. The dc-motor is controlled by a dedicated digital controller which takes feedback from an optical encoder mounted on the shaft of the motor. The encoder produces two sets of ttl-pulses, one every 0.5° of rotation and one every full rotation. The whole system leads to minimum vibration of the disk and a constant rotation speed to within 0.003%. The measurement surface consisted of a 3.175 cm thick, 45.72 cm diameter aluminium disk. The disk was ground and diamond lapped to be flat and parallel to 0.0038 mm. The surface of the disk was polished to a 2 μm finish. A photograph of the rotating disk setup, and coordinate frame are shown in figure 1.

A motorized traversing mechanism was mounted above the surface of the disk. It allowed two directions of motion: radial and wall normal, with an accuracy of 0.025 mm and 0.00025 mm respectively. Motion was controlled through software by the digital data acquisition and control (DAC) computer.

Special care was taken to accurately position the hot-wire sensor above the surface of the disk. For this we utilized a cathetometer which was a magnifying telescope with a graticule. This was mounted on a slider which was translated in the vertical direction with a micrometer. The total resolution of the system was 0.002 mm. We determined the distance of the sensor from the disk as one-half the distance between the sensor and its reflection off of the surface.

The surface roughness consisted of small ink dots which were applied in a pattern on the surface of the disk. In order to protect the disk surface, a 0.0254 mm (1 mil) thick kapton film was first applied. The film was affixed to the measurement surface

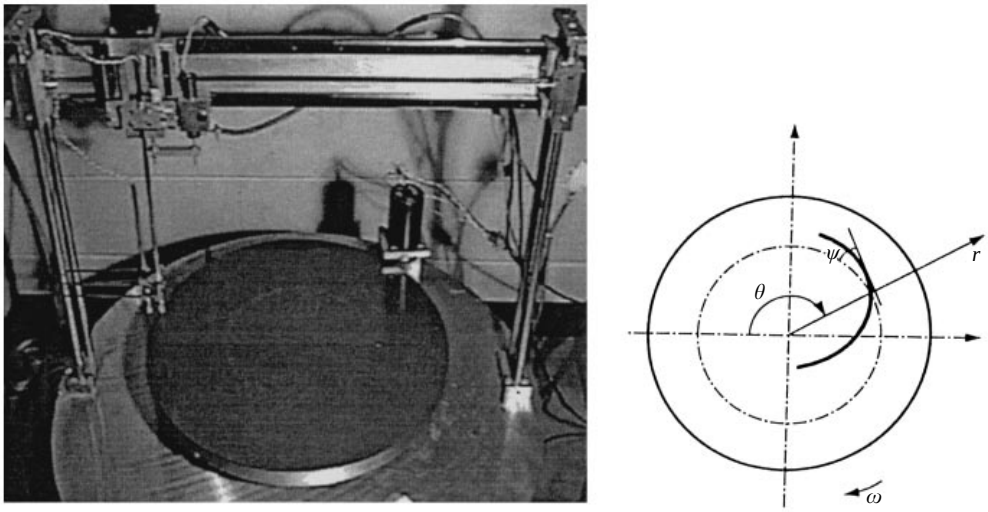

FIGURE 1. Photograph of rotating disk setup (left) and schematic showing coordinate system.

of the disk with a soap and water mixture. Most of the mixture, and any air bubbles, were forced out from under the film. After drying, it left a surface which was as good as the original polished aluminium.

The ink dots were applied with a drafting pen. The pen was mounted on the traversing mechanism using a custom-designed holder. In order to place dots at different azimuthal positions, a friction wheel driven by a stepper motor was mounted to contact the outer edge of the disk. The motor can be seen to the right of the disk in the photograph in figure 1. During the experiment, the friction wheel was disengaged.

The rotational placement of the dots used the 0.5° optical pickup on the disk position feedback for gross positioning. Fine positioning used the stepper motor calibration. The azimuthal resolution in dot placement was determined to be 0.053°. The location of the dots was always referenced to the same rotational position on the disk. This position also corresponded to the first point in a velocity data acquisition time series.

To obtain velocity measurements, a constant-temperature hot-wire anemometer was used. The hot-wire probe was mounted in the traversing mechanism and positioned under computer control. The sensor was oriented so that it would primarily sense the azimuthal velocity component, U_θ.

The anemometer output was divided into AC and DC signals. The AC signal was obtained by passing the analog signal through a band-pass filter with frequency cutoff settings to remove the DC ($\geqslant 0.1$ Hz) and to prevent digital aliasing. It was then amplified to use the full range of the A/D converter and thereby minimize digital quantization error. The DC containing signal was separately d.c.-shifted and amplified. Following this analog conditioning, the AC and DC signals were input to an A/D converter in the DAC.

An additional signal was obtained from the optical sensor which marked each complete rotation of the disk. The time duration of each pulse was short. In order to guarantee that the pulse train could be properly detected when digitized, the pulses were lengthened and sharpened by passing them through a timing circuit before being input into the A/D converter.

Input conditions

ω	104.7 s^{-1}
$R_c = r_c \left(\omega/\nu\right)^{1/2}$	285 (theory)
r_c	11.1 cm

Measurement locations (r/r_c)

0.69	0.78	0.92	1.01	1.10	1.18	1.27
1.35	1.39	1.47	1.50	1.59	1.62	1.70
1.73	1.82	1.85	1.93	1.96	2.05	

Periodic roughness conditions

Roughness type	r/r_c	n
'Clean/kapton'	—	—
1	0.96	19-spiral
2	1.21	27-dot

TABLE 1. Experimental conditions

2.2. *Time-series analysis*

The velocity measurements consisted of digitally sampled voltage time series proportional to the azimuthal velocity (U_θ). A total of 32 contiguous time series (records) were acquired at 21 discrete points in the wall-normal (z) direction for 20 radial (r) locations. The radial locations were upstream and downstream of the critical radius (r_c), which corresponded to the minimum critical Reynolds number ($R_c = 285$) based on linear theory. The disk rotation speed was fixed at $\omega = 104.7$ s^{-1}. The contiguous records were 1024 points in length which corresponded to 6.82 revolutions of the disk. The beginning of the data acquisition was initiated by the pulse from the optical sensor on the disk. Thus the first point in every time series corresponded to the same rotation position of the disk. A summary of the experimental conditions is given in the top part of table 1.

To ensure that an integer number of time series points was acquired for each disk rotation, the data acquisition frequency was chosen so that it would evenly divide into the D/A clock frequency, and the disk rotation frequency evenly divided into the data acquisition frequency. For a clock frequency of 800 kHz and a disk rotation frequency of 16.667 Hz, a sampling frequency of 2.5 kHz was chosen. This gave 150 points per disk revolution, allowing us to resolve stationary modes with azimuthal mode numbers (n) of up to 75. This was more than twice as high as we expected to see, based on linear theorys predictions.

The time-series processing consisted of converting the digitized hot-wire anemometer voltages to velocities using a fourth-order polynomial calibration equation. The polynomial coefficients were determined during calibration runs by a least-squares fit against known velocity points. The calibrated velocity time series were stored along with the simultaneously sampled pulse train corresponding to each rotation of the disk.

A number of time series processing steps were taken. The simplest of these was calculating the time-averaged mean values which were used in the determining the mean velocity profiles.

One of our principle objectives was to separate the velocity fluctuations in the time series into contributions from stationary and travelling instability modes. To do this,

we first constructed the rotation-averaged time series. This corresponded to averaging together the velocity series of successive rotations of the disk. Here we utilized the sampled pulse train marking each rotation of the disk to ensure that the points in each ensemble started and ended in a full rotation of the disk. We also verified that the number of sampled points for a complete rotation of the disk was the proper amount. At the acquisition frequency of 2500 Hz, and disk rotation rate of 16.667 Hz, we expected 150 points/rotation. With 1024 points in 32 records, the ensemble was made up of 192 averages.

To obtain the part of the time-series fluctuations due to travelling modes, the rotation-averaged series was subtracted from each 150-point segment of the total time series. This process was performed for each sampled spatial point in all the cases.

Having separated the time series into those corresponding to stationary and travelling types, frequency analysis was done by calculating the auto- and cross-spectra, and cross-bicoherence. These utilized discrete fast Fourier transforms (FFT) and record averaging to obtain converged statistics. The typical FFT size was 128 points. This gave a frequency resolution of 19.5 Hz, or for stationary modes $\Delta n \simeq 1$. Amplitudes corresponding to spectral peaks were converted to r.m.s. by taking the areas under the peaks and normalizing them by the frequency band width. These were used to determine the spatial amplitude distributions for particular modes.

The method of calculating the cross-bicoherence followed that of Corke, Shakib & Nagib (1991, Appendix B). The cross-bicoherence is a measure of the phase locking between frequencies in two time series and the sum and difference frequency in a third time series, $\theta(f_1) \pm \theta(f_2) = \theta(f_{1\pm2})$. Such a triple phase locking is one of the two requirements needed to confirm a triad resonance. The other necessary condition is wavenumber matching which requires using two probes in two spatial arrangements to determine the two-dimensional wavenumber vector. This analysis is presented in a forthcoming paper (Corke & Matlis 1997). In the present work, we examined only the triple phase locking that existed between frequencies in the time series corresponding to travelling modes, to produce sum and difference frequencies in the stationary-mode time series.

2.3. *Dot conditions*

In total we examined seven different roughness conditions (Knasiak 1996). The results presented here correspond to three of these. These are summarized in the bottom part of table 1. Here, 'clean/kapton' refers to the aluminium disk covered by the kapton sheet, without dots applied. To verify that the kapton sheet covering did not alter the instabilities on the disk, we also documented the bare aluminium disk. The results showed no important differences so that the 'clean/kapton' condition became the base or uncontrolled case in the experiment.

The other cases correspond to equally spaced dots at a single radius (designated 'dot') or logarithmic spirals ('spiral'). In each of the cases, the azimuthal number of dots and the radius where they were placed was intended to enhance particular azimuthal wavenumbers of stationary cross-flow modes. The azimuthal mode number, n, of stationary waves was expected to vary linearly with Reynolds number (R) according to $n = \beta R$ (Malik *et al.* 1981), where $\beta = 0.0698$ is the azimuthal wavenumber. For a fixed rotation speed, $r \propto R$. For the 19-spiral case, placed at $r/r_c = 0.96$, the azimuthal number of dots was intended to reinforce both the most amplified number of of stationary modes, and spiral angle ($\psi = 11.2°$). The other case with 27 dots at $r/r_c = 1.21$ would not excite the most amplified mode.

(*a*)

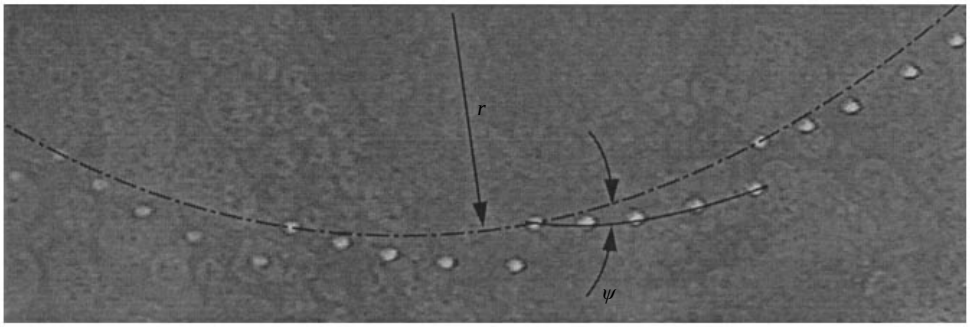

(*b*)

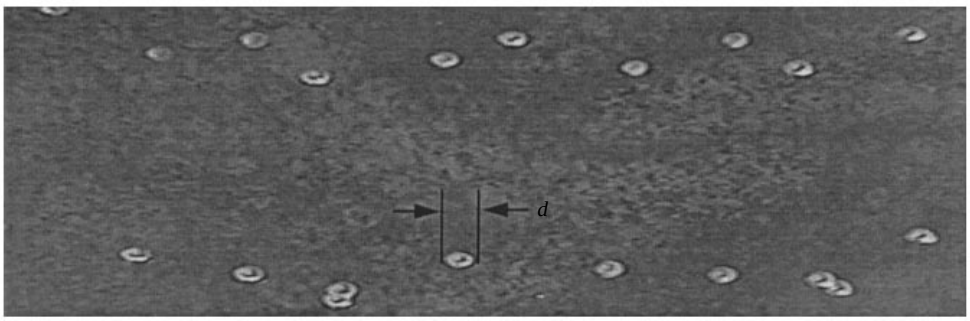

$d = 1.6$ mm $\quad h = 0.06$ mm $\quad h(\omega/\nu)^{1/2} = 0.16$

FIGURE 2. Close-up photographs of ink dot patterns: (*a*) the spiral dot arrangement; (*b*) an enlarged view demonstrating repeatability of the dots.

Figure 2(*a*) shows a photograph of the spiral dot arrangement. The interior dots fall on a prescribed radius, r. Only the interior points would be applied in a 'dot' case. With a 'spiral' case, the spiral angle was formed by having a series of dots which follow a logarithmic spiral with the local angle ψ. For the 19-spiral case, the extent of the dots forming the spiral was $0.955 \leqslant r/r_c \leqslant 1.005$.

Figure 2(*b*) shows an enlarged view of a random region of dots. This is meant to demonstrate the degree of repeatability we achieved in the shape and size of the dots. The diameter of the dots was 1.6 mm. Their height was 0.06 mm. The dimensionless height of the dots was $h(\omega/\nu)^{1/2} = 0.16$. The dots were not hemispherical in shape but rather took on a 'doughnut-shape' after drying.

3. Results

3.1. *Basic flow*

It was our objective that the dots applied to the surface of the disk act to excite a narrow band of cross-flow modes, but otherwise do not directly change the mean flow. As a check on this, we documented the mean velocity profiles in all the cases, with and without dots. Figure 3 shows the mean velocity profiles at different radial positions for the 27-dot case. The profiles are shown with the similarity wall

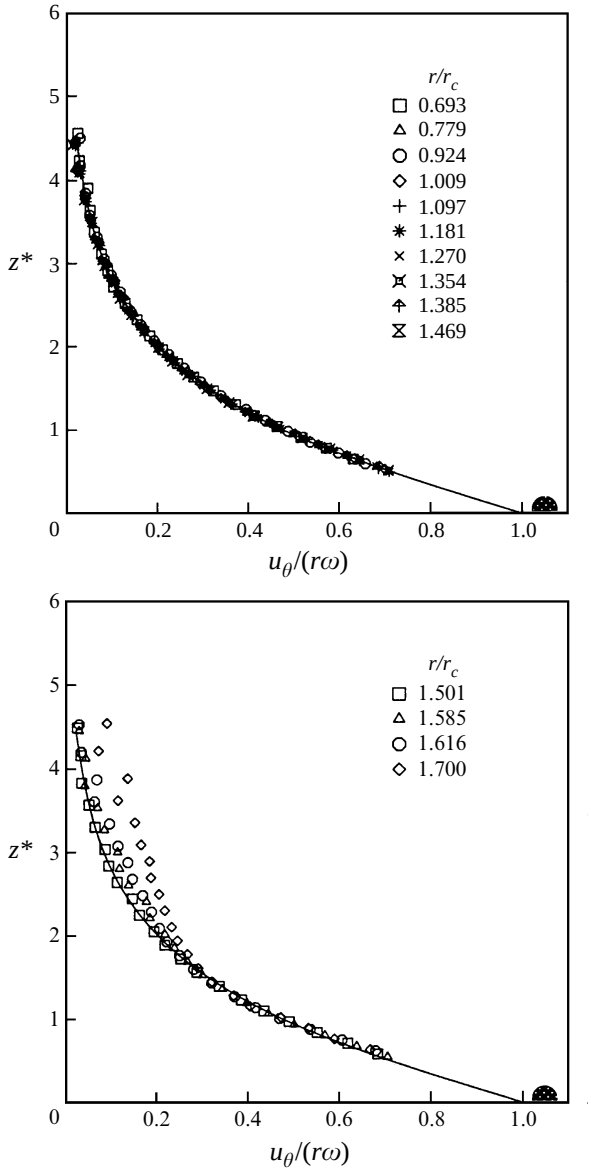

FIGURE 3. Mean velocity profiles at different radial positions for the 27-dot case.

distance, $z^* = z(\omega/\nu)^{1/2}$, and the similarity azimuthal velocity, $u^* = u_\theta/(r\omega)$. Shown for reference at the right of each plot is the height of a dot in similarity units.

In figure 3, the different symbols correspond to the different radial positions. Recall that the dots in this case are located at $r/r_c = 1.21$. Therefore six of the profiles are inboard of the dots and so serve to document the clean/kapton base condition. The solid curve is the theoretical (laminar) mean velocity profile for an infinite radius rotating disk. The results show an excellent agreement with the theoretical profile, even well beyond the location of the dots. The mean velocity profiles only begin to deviate when the amplitude of the cross-flow modes reach a sufficient level to distort

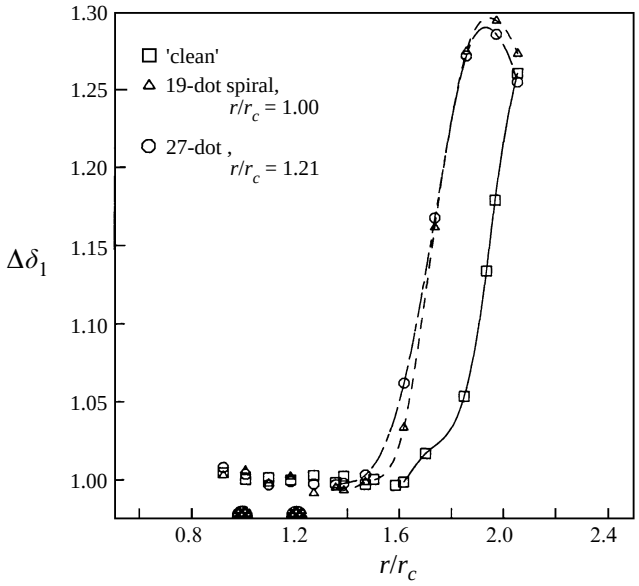

FIGURE 4. Radial change in displacement thickness for the three cases: clean/kapton, 19-spiral and 27-dot.

the mean flow. In this case, this occurs for $r/r_c > 1.5$. This insensitivity of the mean flow to the immediate presence of the dots is typical of all the cases (Knasiak 1996).

One of the advantages of the rotating disk is that for a laminar flow, the boundary layer thickness is constant. Therefore the radial position where the boundary layer thickness changes marks the location where nonlinear effects (mean flow distortion) begin. This is demonstrated in figure 4 which shows the variation in the displacement thickness with radial position. Here $\Delta\delta_1$ is the ratio of the local displacement thickness to the average thickness in the laminar region ($r/r_c \leqslant 1.4$). The three cases are shown in the plot. For the two cases with dots, the symbols at the bottom of the figure mark their respective locations.

All three cases show that the displacement thickness remains constant over a large portion of the disk. This region extends well past the location of the dots, which indicates that their initial effect is linear. The rise in the displacement thickness marks the beginning of the nonlinear region. This point occurs at a larger radius for the clean/kapton case. There is only a small difference in this position between the two dot cases. On subsequent figures, the end of the linear region will be indicated by reference to this figure as the location where the displacement thickness first deviates from the initial constant value.

3.2. *Stationary modes*

Having decomposed the total time series fluctuations into those due to stationary and travelling types, we focus here on the characteristics of the stationary cross-flow modes. As discussed in §2, the stationary mode time series is an ensemble average of the velocity fluctuations occurring over successive rotations of the disk. Those fluctuations which are not repeatable from one rotation to the next are averaged out. The ensemble average was constructed for all the spatial points $(z, r/r_c)$.

A set of ensembles is shown in figure 5 for the clean/kapton case. These are presented for different r/r_c locations at a fixed height above the disk surface of

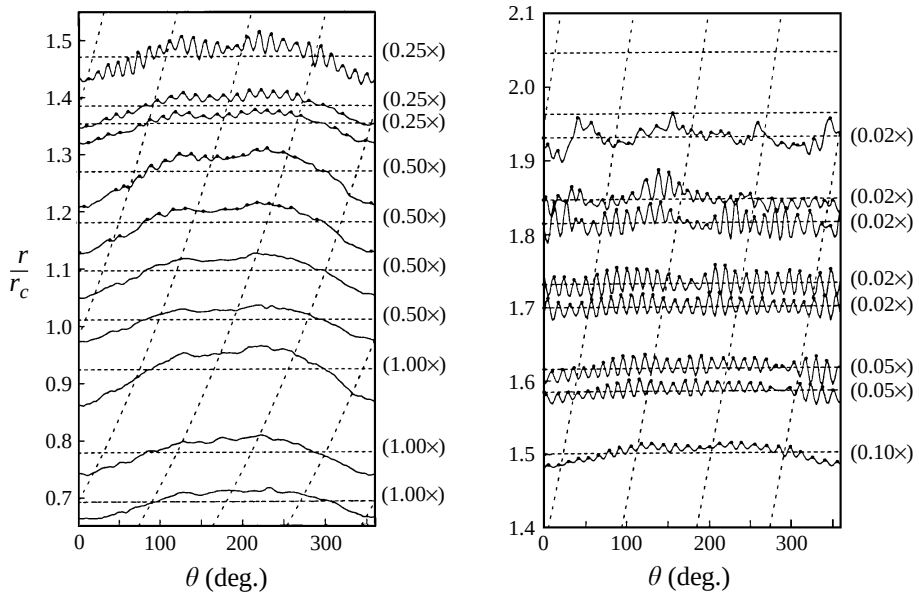

FIGURE 5. Rotation-averaged velocity fluctuations at different radial positions for the clean/kapton case. $z^* = 1$. Dots mark peaks of fluctuations corresponding to stationary cross-flow waves.

$z^* = 1$. The abscissa shows the disk rotation angle, making up one complete rotation. On the left ordinate, the horizontal dashed lines mark the r/r_c locations of each trace. For presentation purposes, the traces have been magnified by different amounts. The magnification values used are given on the right ordinate.

Focusing on this figure, we observe the development of a periodic component which appears past the critical radius. We associate these fluctuations with Type 1 stationary cross-flow modes. These are significantly amplified in the radial direction, which is evident from the rapidly decreasing magnification factors for the traces. The dots on the traces in the figure mark the locations of 'peaks' in the periodic velocity fluctuations. Each peak corresponds to a cross-flow instability wave as it convects past the stationary velocity sensor. The number of peaks per rotation gives the azimuthal mode number, n.

The variation in the azimuthal mode number with radial position is shown for this case in figure 6(a). This was generated by counting the 'peaks' in the stationary mode time traces presented in figure 5. Shown as the solid line is the relation $n = \beta R$ with $\beta = 0.0698$. Here β is the instability wavenumber in the θ-direction. As pointed out by Malik *et al.* (1981) for linear stability calculations, β is nearly constant with R so that n should vary nearly linearly with R with a slope $\simeq \beta$. The dashed line represents a linear fit to the data. The slope of the line gave a value of $\beta = 0.0796$. Regardless of β, the most amplified radial wavenumber, α, remains essentially the same (0.354). Therefore the value of β determines the trajectory angles of the cross-flow modes ($\psi = \tan^{-1}(\beta/\alpha)$). For the clean/kapton case in figure 6(a), $\psi = 12.35^\circ$. For such clean disks, values between 11°–14° are usually cited (Malik *et al.* 1981; Faller, 1991).

Referring back to figure 5, the curved dashed lines correspond to logarithmic spiral trajectories with a local angle of $\psi = 12.35^\circ$. Here we are looking to see how well this trajectory connects peaks (or valleys) in the traces from one radius to the next. In general it connects them well, giving us confidence in our determination of β.

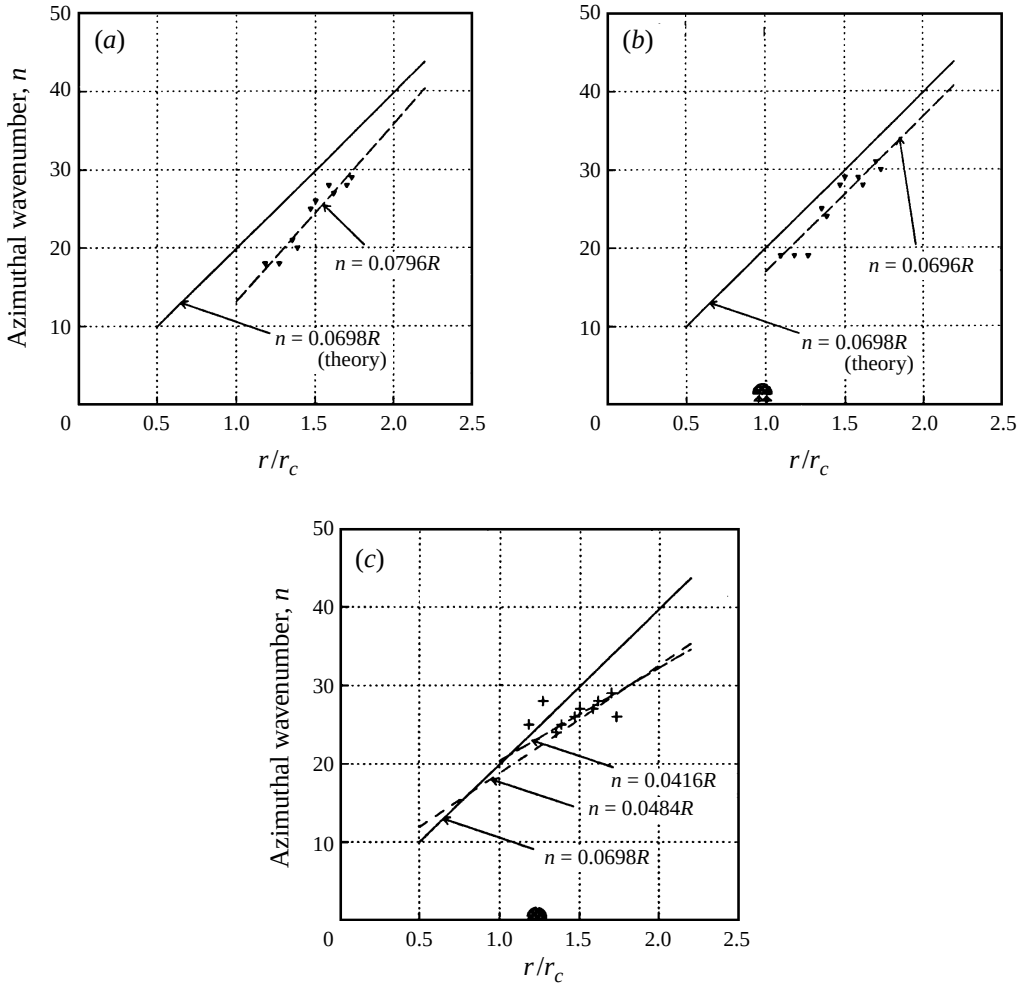

FIGURE 6. Radial variation of azimuthal mode number for (*a*) the clean/kapton, (*b*) 19-spiral and (*c*) 27-dot cases.

The variation in the azimuthal mode number with radial position for the other two cases is shown in figures 6(*b*) and 6(*c*). The 19-spiral case was intended to produce waves at the most amplified condition of $\beta = 0.0698$, or $\psi = 11.2°$. Figure 6(*b*) verifies that this was achieved. In contrast, the 27-dot case in 6(*c*) was designed to produce waves which were off the most amplified condition. In this case the points fall on a straight line with a value of $\beta = 0.0416$. This is shown as the long-dashed line. This case had been previously studied in a different facility (that of Wilkinson & Malik 1985) by Corke & Knasiak (1994). That result is indicated by the short-dashed line and gave $\beta = 0.0484$. This approximately 8% difference is a good indication of the repeatability of the this result. Replicating the 27-dot case in the same disk setup as us, Matlis (1997) determined nearly the same value of $\beta = 0.0418$. He used a different method which used two simultaneously sampled sensors to determine the local wavenumber vector. Using the present value of $\beta = 0.0416$, the corresponding spiral angle is $\psi = 6.7°$. As with the clean/kapton case, the values of ψ in these two

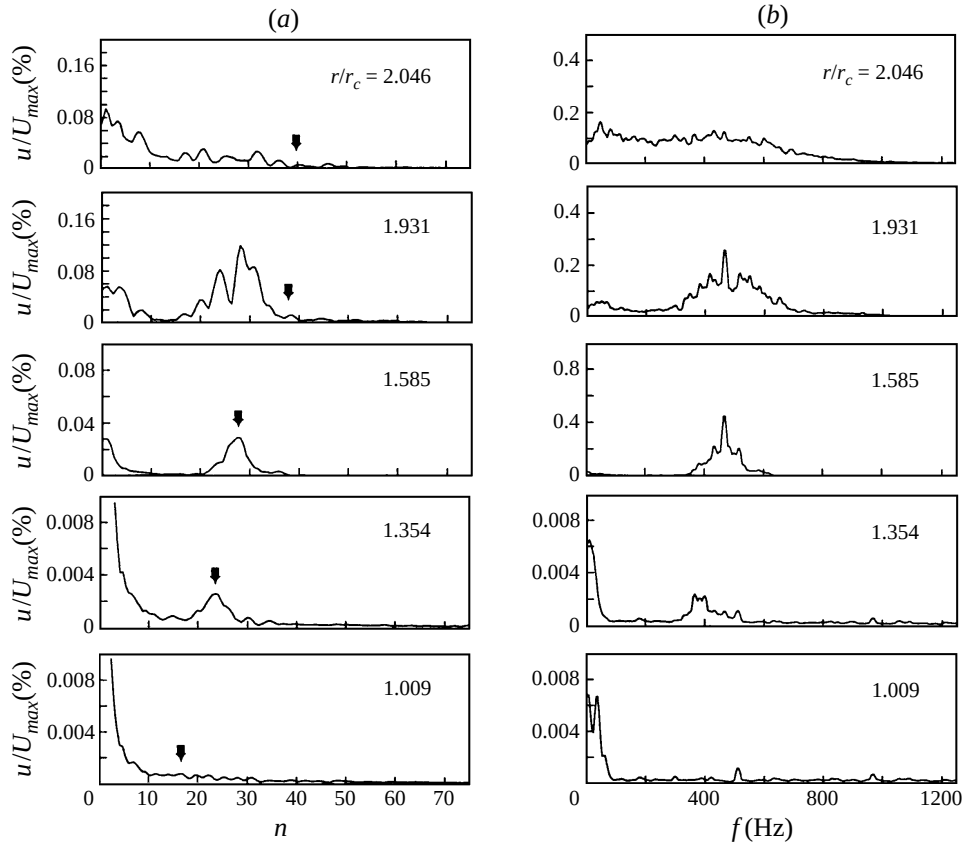

FIGURE 7. Spectra of velocity fluctuations at different radial positions for (*a*) stationary and (*b*) travelling cross-flow modes in clean/kapton case.

cases were found to give logarithmic spirals which fit well the locations of the peaks in successive radii of stationary mode traces (Knasiak 1996).

3.3. *Mode development*

The previous results in figures 5 and 6 were based on counting time-series 'peaks' which we associate with the stationary cross-flow modes, and the use of $n = \beta R$ which comes from linear stability theory. In this approach we have focused on all fluctuations, without regard to their amplitudes. In order to take into account the amplitudes of the fluctuations, we present velocity spectra. These are shown for the clean/kapton case in figure 7 for five different radial positions, which span the linear and nonlinear regions, at $z^* = 1$. Figure 7(*a*) shows spectra for the time series representing stationary modes. In this case the frequency has been divided by the disk rotation frequency so that the axis is in terms of the azimuthal mode number, *n*. Figure 7(*b*) shows spectra for the time series representing travelling modes. In this case it is not appropriate to normalize by the disk rotation speed, so the frequency axis is in Hz.

At any supercritical radii, we expect to see a range of mode numbers which represent the progression of growing and decaying cross-flow waves so that *n* varies linearly with radius. The spectra should then appear as a relatively smooth 'band' which is moving to progressively higher frequencies (or *n*) as r/r_c increases. For the stationary

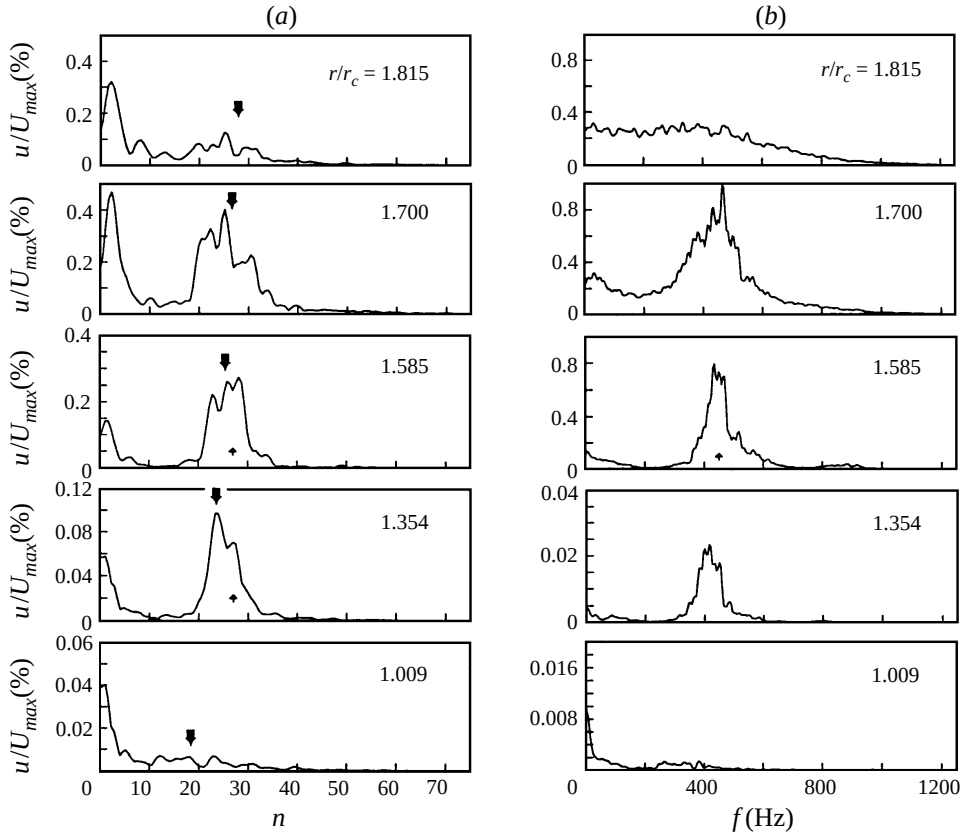

FIGURE 8. Spectra of velocity fluctuations at different radial positions for stationary (*a*) and travelling (*b*) cross-flow modes in 27-dot case.

modes in the linear region ($r/r_c \leqslant 1.585$ for the clean/kapton case), this is the case. The bold arrows in figure 7(*a*) correspond to the values of n given by $n = \beta R$ where β was taken from figure 6(*a*). These indicate that within the linear region, $n = \beta R$ represents the largest-amplitude peaks in the spectra. Within the nonlinear region however, the largest-amplitude peaks do not follow $n = \beta R$. Secondly, the spectra in this region show a 'grouping' of frequencies which cannot be explained by linear theory. An example is the multiple narrow peaks that occur at $r/r_c = 1.931$ in this case.

The spectra for the 27-dot case are shown in figure 8 for comparison. The arrangement of the spectra is the same as with figure 7 although different radial positions are shown to account for the shorter linear development region compared to the clean/kapton case. Again the bold arrows correspond to $n = \beta R$. The smaller arrows mark the value of n for this 27-dot case. The second radial position shown ($r/r_c = 1.354$) is slightly outboard of the location of the dots. There we observe a peak in the spectra corresponding to that mode number. However $n = 27$ is not the largest-amplitude peak. The largest peak corresponds to the most-amplified mode number given by $n = \beta R$ (bold arrow). In the nonlinear region ($r/r_c \geqslant 1.587$) we again see a grouping of frequencies into narrow peaks. Also evident is a large peak at $n = 2$. This stationary mode is the most dominant in the spectra at the end of the nonlinear region.

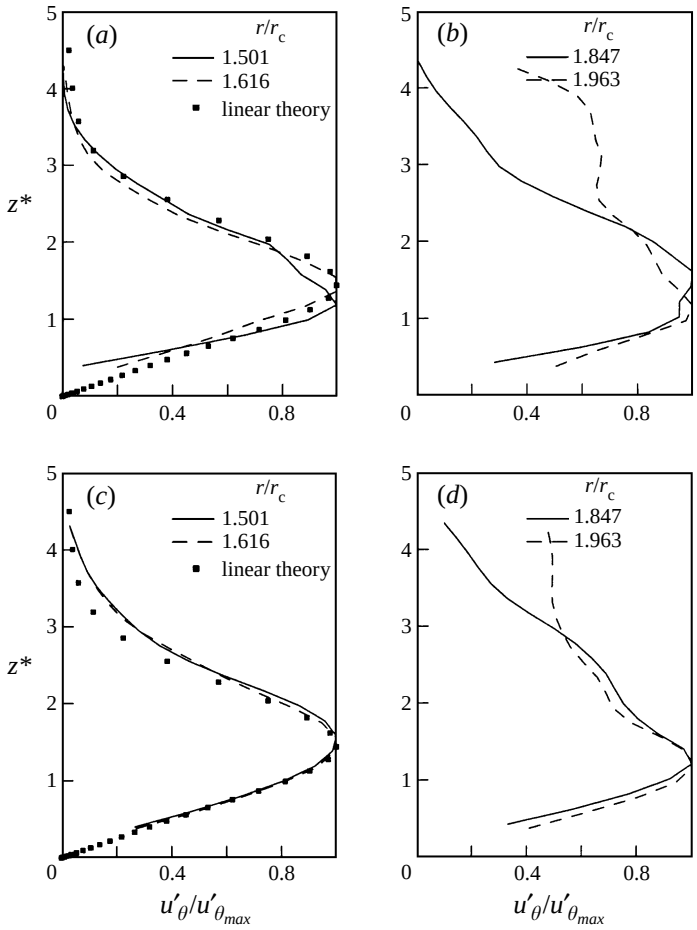

FIGURE 9. Wall-normal amplitude distributions at four radii for $n = 28$ (a, b) and $f = 459$Hz (c, d) of the clean/kapton case. Heavy dotted curve is linear theory eigenfunction.

Focusing on the spectra of the travelling modes for the 27-dot case, shown in figure 8(b), the dots appeared to have focused fluctuations into a relatively narrow frequency band compared to the clean/kapton case. For reference we have placed a small arrow at the frequency corresponding to the product of the dot number and rotation speed ($n\omega/2\pi = 450$ Hz). In this case, although the travelling disturbances have a lower initial amplitude, they grow faster than the stationary disturbances so that they have the highest amplitude going into the nonlinear region.

In order to verify that the peaks in the spectrum correspond to instability modes, we documented their amplitude distributions and compared them to linear stability theory eigenfunctions. This is done for the clean/kapton and 27-dot cases in figures 9 and 10. Each figure shows the wall-normal amplitude distributions at different radial positions. For each case the top set of plots corresponds to a stationary mode, and the bottom set to a travelling mode. Each plot shows profiles at two radial positions which are designated by different line types. The left-hand plot of each set corresponds to the linear region, and the right-hand plot to the nonlinear region. The linear theory eigenfunction is shown as the heavy dotted line. At each radial position,

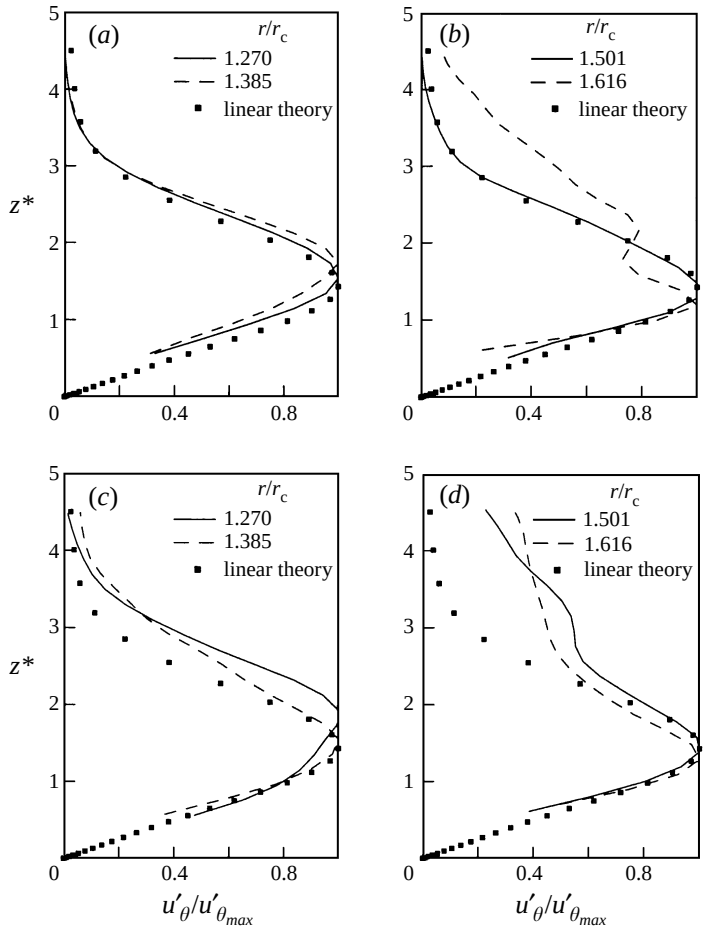

FIGURE 10. Wall-normal amplitude distributions at four radii for $n = 27$ (*a*, *b*) and $f = 427$Hz (*c*, *d*) of the 27-dot case. Heavy dotted curve is linear theory eigenfunction.

the r.m.s. value taken from the spectra at a chosen frequency has been normalized by the distribution maximum so that the shapes could be compared.

The distributions for the clean/kapton case are shown in figure 9. For the stationary mode we chose $n = 28$ which is one of the largest peaks in the spectrum (figure 7*a*). Within the linear region, we observe a good correspondence between the measured and theoretical distributions. In the nonlinear region, the single-peaked distribution develops a second peak away from the wall. This shape agrees with nonlinear distributions obtained in DNS calculations such as those of Joslin & Streett (1994).

For the travelling mode we chose a frequency of 459 Hz. This is near the middle of the broad spectral peak for the travelling modes in figure 7 (*b*). For an $n = 28$ mode it corresponds to a phase speed which is approximately 2% slower than the disk speed. Linear theory for travelling cross-flow modes predicts phase speeds in the range of approximately 15% of the disk speed (Faller 1991). In the linear range, we again observe good agreement between the measured distribution and theory. In the nonlinear region, this takes on a two-peaked distribution which is similar to that of the stationary mode.

The amplitude distributions for the 27-dot case are shown in figure 10. For the

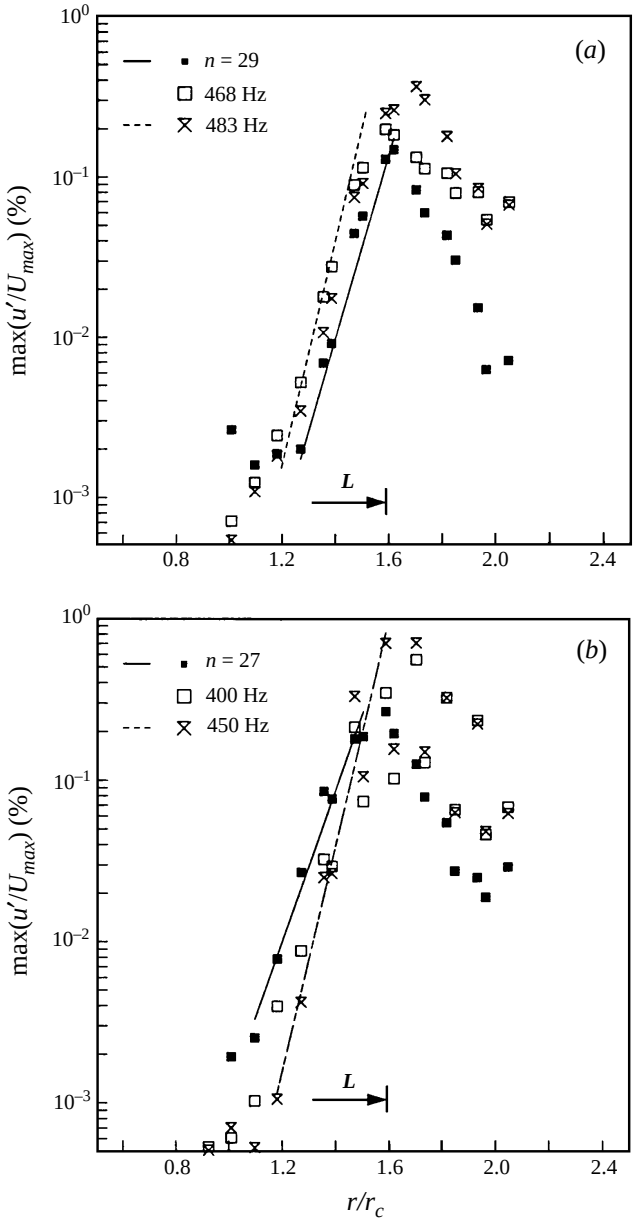

FIGURE 11. Radial growth in amplitude of selected stationary and travelling modes in (*a*) the 19-spiral and (*b*) the 27-dot cases.

stationary mode we chose $n = 27$. The profiles start at a radial position which is just outboard of the dots. In the linear range, the measured distribution shows a similar good comparison to theory. The nonlinear development takes on the characteristic double-peaked distribution. For the travelling mode we selected a frequency of 427 Hz. In this case the comparison with theory is acceptable, although we found slightly larger amplitudes above the peak ($z^* > 2$) compared to the linear eigenfunction. This may be an indication of some early nonlinear effects.

We next document the radial growth in amplitude of the dominant modes in the

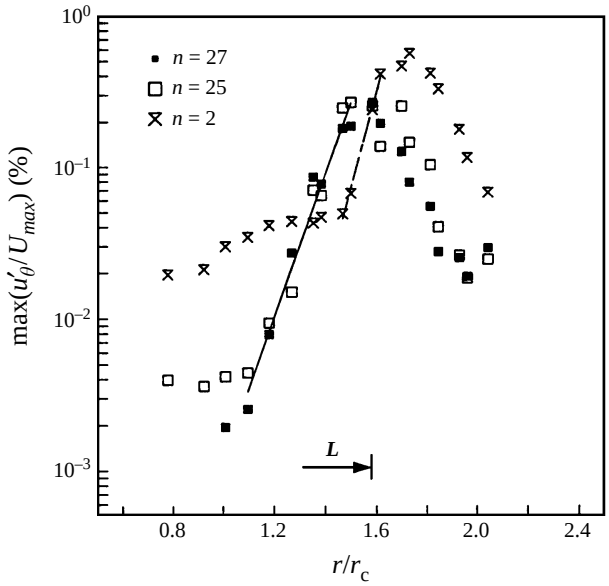

FIGURE 12. Radial growth in amplitude of $n = 2$ mode and comparison to other other stationary modes in the 27-dot case.

two cases with dots. This is shown in figure 11. This was constructed by plotting the maximum amplitude of selected modes (frequencies) at each radial position. As we saw in the previous two figures, this maximum amplitude generally corresponds to $z^* = 1.5$. The amplitude axis is a log scale in order to emphasize exponential growth.

The result for the 19-spiral case is shown in figure 11(*a*). This was included instead of the clean/kapton case because we view it as a controlled 'natural' case which was designed to emphasize the most-amplified modes based on linear theory. Here we selected the stationary mode at $n = 29$ and travelling modes at 468 and 483 Hz. These were most dominant at the end of the linear region based on the spectra. For the three modes in this case, there is a clear linear growth region. The solid and dashed lines represent a linear fit to the data. These are drawn to guide the eye through the points. The slopes of these were used to determine a local amplification rate, α_i. For $n = 29$, $\alpha_i = 0.045$, and for either of the travelling modes at $f = 468$ or 483, $\alpha_i = 0.051$. The larger amplification rate for the travelling waves agrees with linear theory. The value for the stationary mode is in good agreement with Mack (1985) who found the largest growth rate for pure waves to be $\alpha_i = 0.043$.

The result for the 27-dot case is shown in figure 11(*b*). Here we selected the stationary mode at $n = 27$ and two travelling modes at $f = 400$ and 450 Hz. These also show a well defined exponential (linear) growth region. As we expect, being in roughly the same band of frequencies, the amplification rate (slope) of the travelling modes is the same as those in the 19-spiral case. The amplification rate of the $n = 27$ mode of $\alpha_i = 0.034$ is however considerably less than the most amplified. This is because this azimuthal mode number was introduced at a radius where it was not the most amplified.

In either case, the end of the exponential growth coincides well with the end of the linear region, marked by the jump in the displacement thickness documented in figure 4. This location is indicated at the bottom part of each plot. Owing to the larger

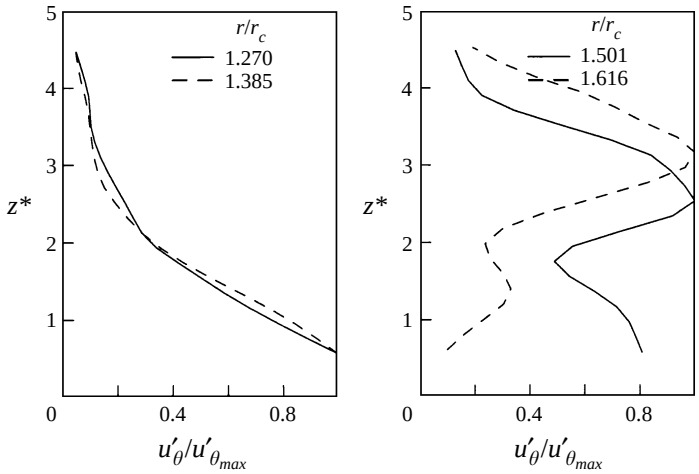

FIGURE 13. Wall-normal amplitude distributions at four radii for $n = 2$ in the 27-dot case.

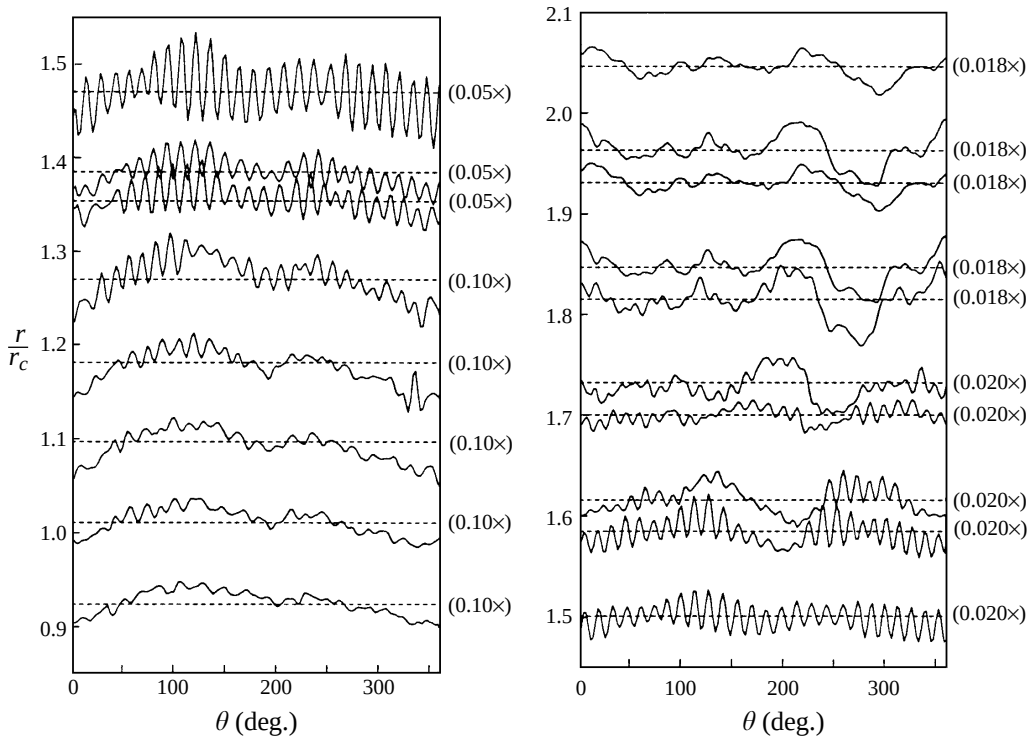

FIGURE 14. Azimuthal variation of the displacement thickness produced by stationary modes in the 27-dot case.

amplification rates, the travelling modes reach a larger amplitude than the stationary mode at energy saturation.

In the nonlinear region, the spectra for the stationary modes in the 27-dot case (figure 8*a*) had shown the growth of a mode at $n = 2$. We look at the radial growth of this mode in figure 12. For reference in this figure, we have also plotted the growth of the $n = 27$ and 25 modes. Here we see that the $n = 2$ mode only shows exponential

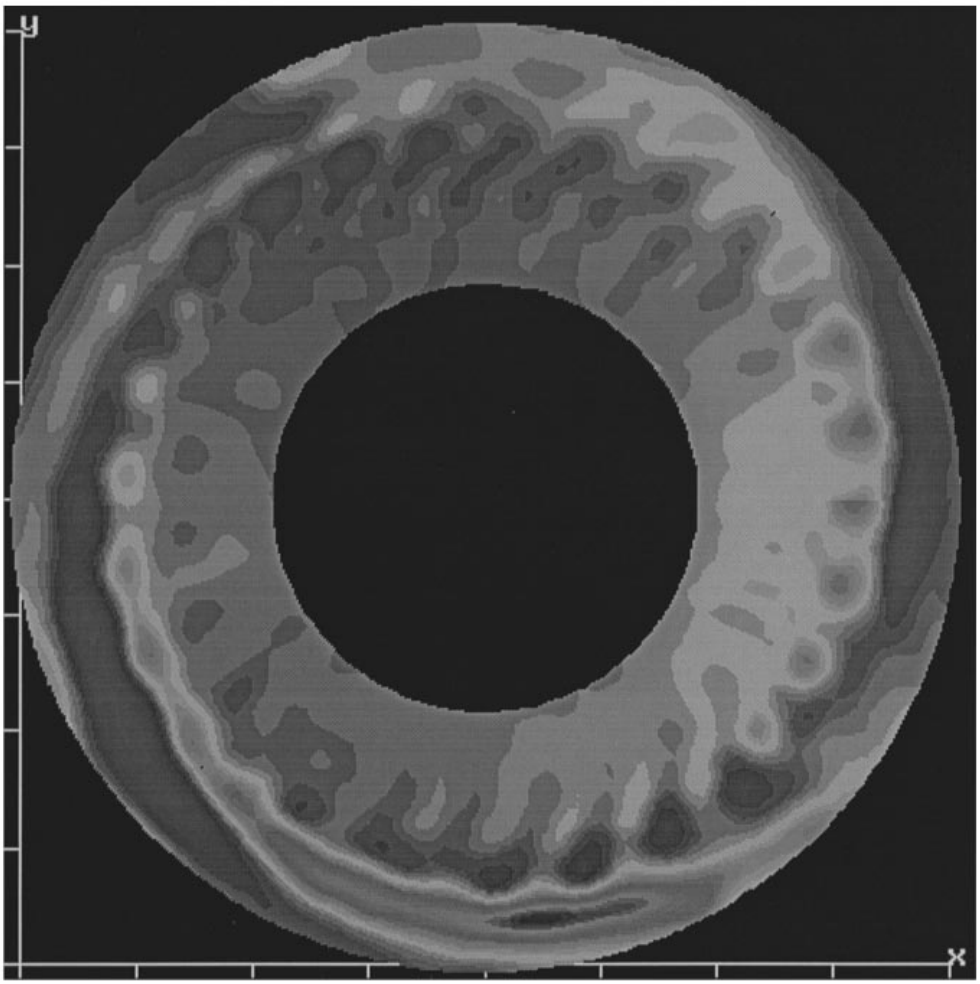

FIGURE 15. Same as figure 14 but drawn as grey-scale isocontours in the cylinder coordinate of the disk.

growth in the nonlinear region. At this point the other dominant stationary modes are decaying so that the largest-amplitude stationary mode at transition is at $n = 2$.

Further information about the $n = 2$ mode comes from viewing its wall-normal amplitude distribution. This is shown in figure 13. The format for these plots is the same as in figure 10. In the linear region shown in the left-hand part of the figure, the amplitude distribution has a maximum at the wall. This distribution is reminiscent of a Stokes oscillating wall layer, and may be the result of any remaining small imperfection in the flatness of the disk surface. When the $n = 2$ mode begins to grow at $r/r_c = 1.501$, the amplitude profile immediately takes on a double-peaked distribution which we associate with a nonlinear mode. The lower peak occurs at $z^* \simeq 1.5$ which is similar to the nonlinear distributions shown for the $n = 27$ mode in figure 10 (right). From such comparisons, we conclude that the $n = 2$ mode is produced by a nonlinear process.

We can see the impact of the $n = 2$ mode on transition by looking at the azimuthal variation of the displacement thickness, $\delta_1(r, \theta)/\overline{\delta_1(r)}$. This is shown in figure 14

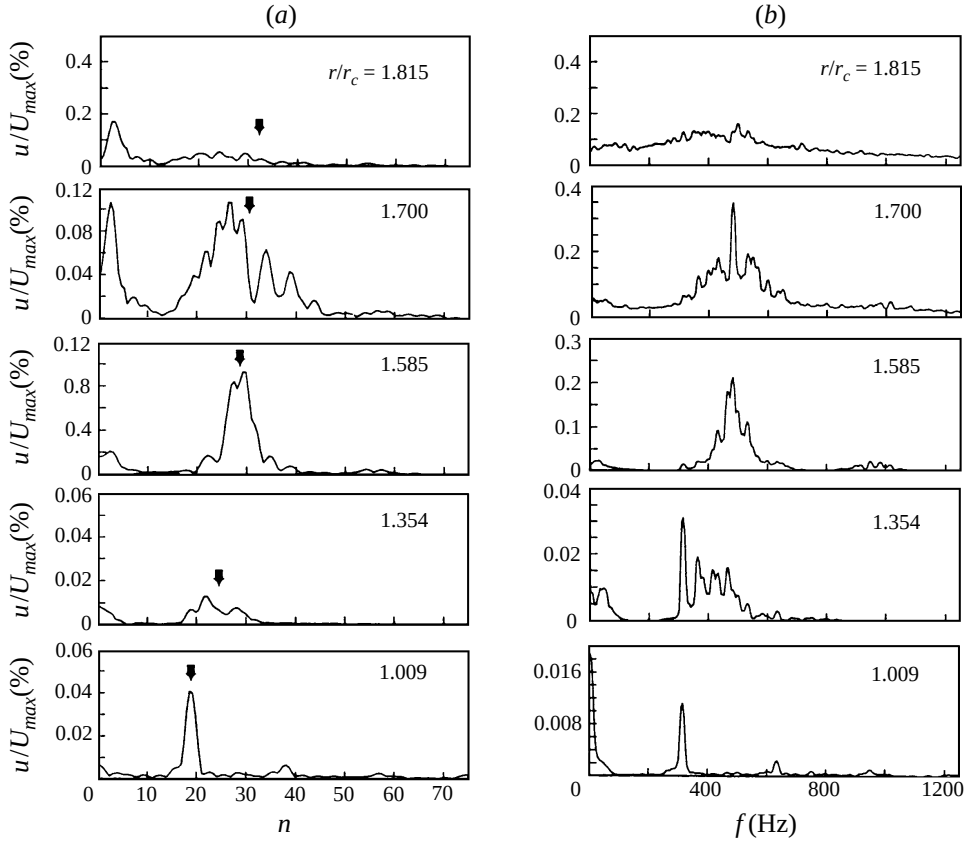

FIGURE 16. Spectra of velocity fluctuations at different radial positions for stationary (*a*) and travelling (*b*) cross-flow modes in 19-spiral case.

for the 27-dot case. This was constructed from the rotation-averaged mean velocity profiles. It is plotted in the same format as the rotation-averaged velocity fluctuations which were presented in figure 5. As before, the r/r_c location and scale factor for each curve are indicated on the left and right axes. We imagine the stationary co-rotating cross-flow vortices, which form in the nonlinear region, to act like 'pumps', bringing the high-momentum fluid from the wall to the outer part of the boundary layer, and low-momentum fluid towards the wall. This results in a distortion of the mean flow in which on one side of the vortex the boundary layer will thin, and on the other side it will thicken. Thus moving around the disk at a fixed radius we expect to see a periodic thickening and thinning of the boundary layer which coincides with the number of stationary modes. This is precisely what we observe in figure 14. In the region $1.3 \leqslant r/r_c \leqslant 1.5$, we observe a higher frequency variation which corresponds to $n = 27$ and higher. At $r/r_c > 1.58$ we observe the growth of a lower frequency with a mode number of $n \simeq 2$.

We can see this somewhat better by plotting the displacement thickness variation in the cylindrical coordinate of the disk. This is shown in figure 15 where the displacement thickness values are shown as constant level grey-scale contours. The darker shaded regions correspond to where the displacement thickness is less than the mean. The lighter shaded regions are where it is greater than the mean. The $n = 2$

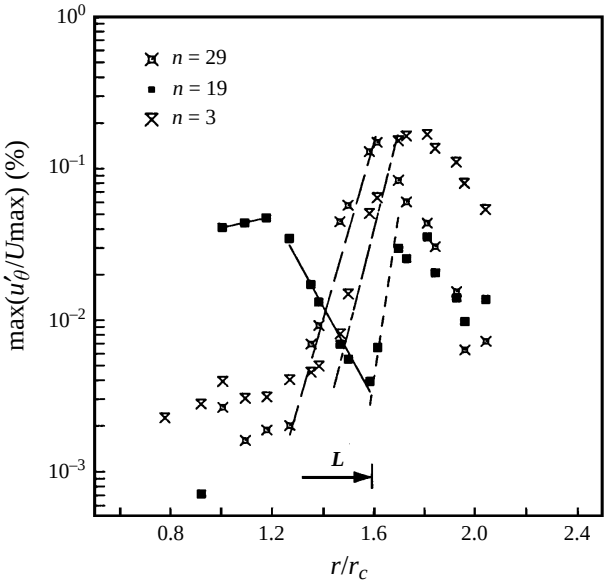

FIGURE 17. Radial growth in amplitude of the $n = 3$ mode and comparison to other stationary modes in 19-spiral case.

variation is clearly visible as the two alternating light/dark regions around the disk at the outer radii.

To show that this is not a unique feature of this case, we consider the 19-spiral case, the spectra for which are presented in figure 16. The format for this is identical to that of the other two cases which were previously shown in figures 7 and 8. Focusing on the stationary modes in the nonlinear region ($r/r_c \geqslant 1.585$), we again observe the multiple narrow spectral peaks, and the emergence of a low-number stationary mode. In this case however, it occurs at $n = 3$.

We document the radial growth of this mode in figure 17, along with that of the $n = 19$ and 29 modes. The dot spirals end at $r/r_c = 1.005$. Following that position, we observe a jump in the amplitude of $n = 19$. This mode appears to saturate and decay to a minimum level at $r/r_c \simeq 1.6$. For reference, $n = 29$ shows an extended exponential growth region until it saturates at $r/r_c \simeq 1.6$. The $n = 3$ mode is the last to grow, beginning in the nonlinear region which starts at $r/r_c \simeq 1.4$, based on the rise in displacement thickness previously presented in figure 4. Also within the nonlinear region we observe a regrowth of the $n = 19$ mode.

We see the impact of the growth of the $n = 3$ mode in the 19-spiral case in the rotation-averaged displacement thickness which is shown in figure 18. The format is identical to that for the 27-dot case shown in figure 15. At the outer radii we can clearly see three alternating light/dark regions which correspond to a $n = 3$ variation in the displacement thickness.

3.4. *Triad-mode interaction*

What accounts for the growth of these low-number stationary modes in the nonlinear regions in these cases? To answer this we considered the possibility of a nonlinear interaction between travelling and stationary modes. To quantify this, we calculated the cross-bicoherence (cbc). The cbc is a measure of phase locking between three modes such that the ensemble-averaged phase between the modes ($\theta(f_i)$) satisfies

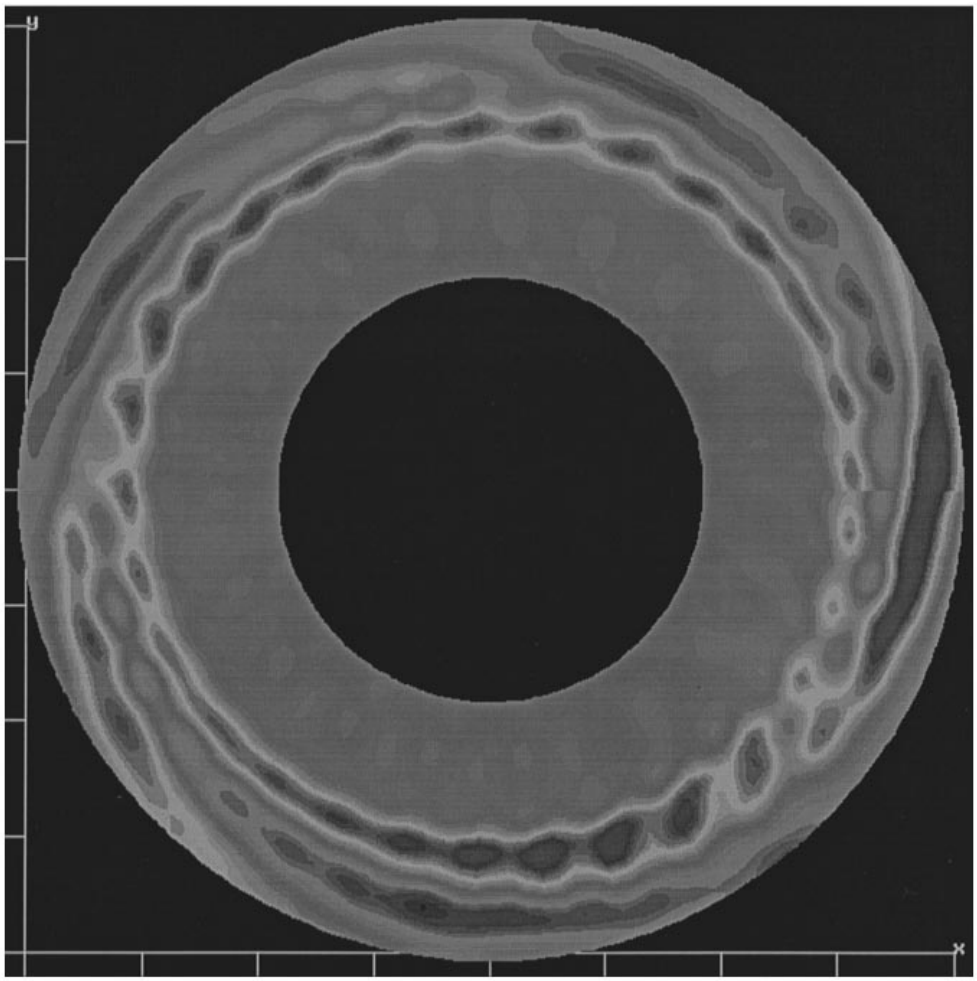

FIGURE 18. Variation of the displacement thickness produced by stationary modes in 19-spiral case.

$\theta(f_1) \pm \theta(f_2) = \theta(f_{1\pm2})$. The cbc is a normalized quantity, where cbc=1 represents perfect phase locking, and cbc=0 indicates no phase locking. Such a triple phase locking is a necessary condition for a three-mode (triad) resonance.

The cbc for the 19-spiral case are presented in figures 19 and 20 for $r/r_c = 1.585$ and 1.700, respectively. Both are at $z^* = 1$. The first radial position is near the beginning of the nonlinear region where $n = 3$ begins to grow. The other is just inboard of the point of amplitude saturation.

The valid region of interacting frequencies forms two triangles. The upper triangle corresponds to summing interactions. The bottom triangle corresponds to difference interactions. Because the cbc involves three frequencies, it requires three frequency axes. In our case, the horizontal and vertical axes corresponds to frequencies of travelling modes. The third frequency is read as a point of intersection with the horizontal axis of a line drawn parallel to the right-hand side of the upper triangle or left-hand side of the lower triangle. Here, the third axis refers to frequencies of stationary modes so that it can be divided by the disk rotation frequency (16.667 Hz) to obtain the azimuthal mode number n. The cbc-levels are drawn as filled contours,

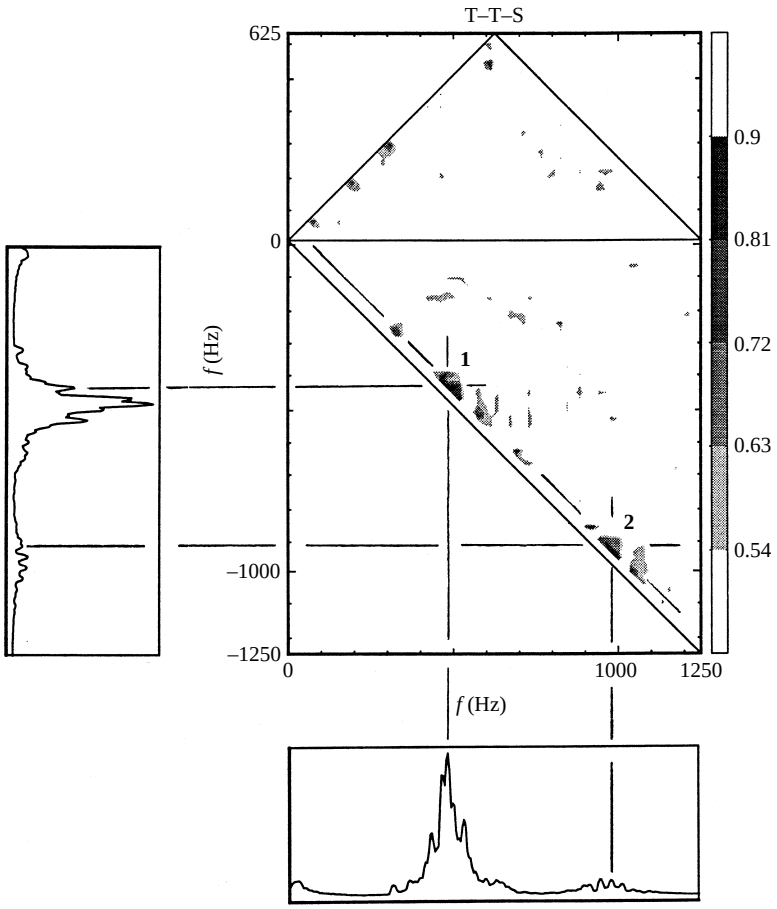

FIGURE 19. Cross-bicoherence for travelling–travelling–stationary mode interaction for the 19-spiral case at $r/r_c = 1.585$ and $z^* = 1$.

with the contour scale shown on the right-hand edge of the plot. We only show the most significant cbc levels. For reference, we have also added the spectra for the travelling disturbances along their respective axis edges.

In general, the cbc show significant phase locking between a number of travelling and stationary modes. In particular, some of the most significant involve difference interactions between the largest-amplitude travelling modes and their frequency side-bands, and the stationary mode at $n = 3$. We have highlighted these by the lines drawn from the spectra.

At the first position of $r/r_c = 1.585$ in figure 19, all the significant interactions involve the $n = 3$ mode. The most important of these is labelled as cbc peak 1. This involves a difference interaction between the largest-amplitude travelling mode and a travelling mode at a lower sideband frequency. The other significant interaction is labelled cbc peak 2. This involves the small harmonic of the primary band of travelling modes seen on the spectrum. It is at approximately this radial position that the $n = 3$ mode begins to grow. At this location, the amplitude of the interacting travelling modes is approximately 10 times that of the $n = 3$ mode, so that we expect that energy would flow from the travelling modes to the stationary mode at $n = 3$. This can account for the growth of the $n = 3$ mode in the nonlinear region.

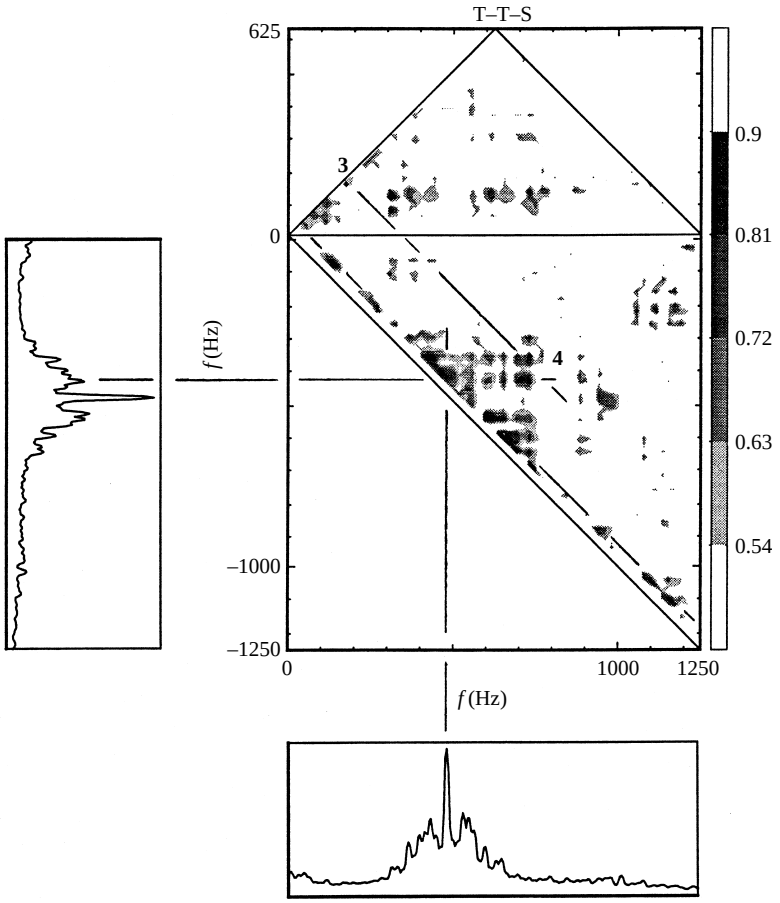

FIGURE 20. As figure 19 but at $r/r_c = 1.700$.

This mechanism is not limited to the lowest azimuthal mode numbers. In the cbc at $r/r_c = 1.585$ we note that there are no significant interactions involving the $n = 19$ mode. This location was just upstream of where the $n = 19$ mode began to regrow (figure 17). However the cbc at $r/r_c = 1.700$ in figure 20 show both a summing and difference interaction between travelling disturbances and the $n = 19$ mode. The peaks in the cbc associated with this are labelled 3 and 4. This suggests that the regrowth of the $n = 19$ mode is due to an interaction with pairs of travelling modes. The amplitudes of these travelling modes are not near the largest, so that the $n = 19$ mode will not be as dominant as the $n = 3$ at the end of the nonlinear region.

We also find interactions involving other stationary modes for example at $n = 29$, 50 and 58. The latter is the third harmonic of $n = 19$. Again, these involve lower-amplitude travelling mode components so that these stationary modes are not dominant in the nonlinear region. However these interactions can account for the multi-peaked character of the stationary mode spectrum that occurs in the nonlinear region.

At this further outboard position there are also many frequencies of travelling disturbances which are phase locked with the $n = 3$ mode. This reflects a broadening of the band of frequencies in the larger-amplitude fluctuations of travelling disturbances. At this radial location the $n = 3$ mode is the largest-amplitude stationary mode,

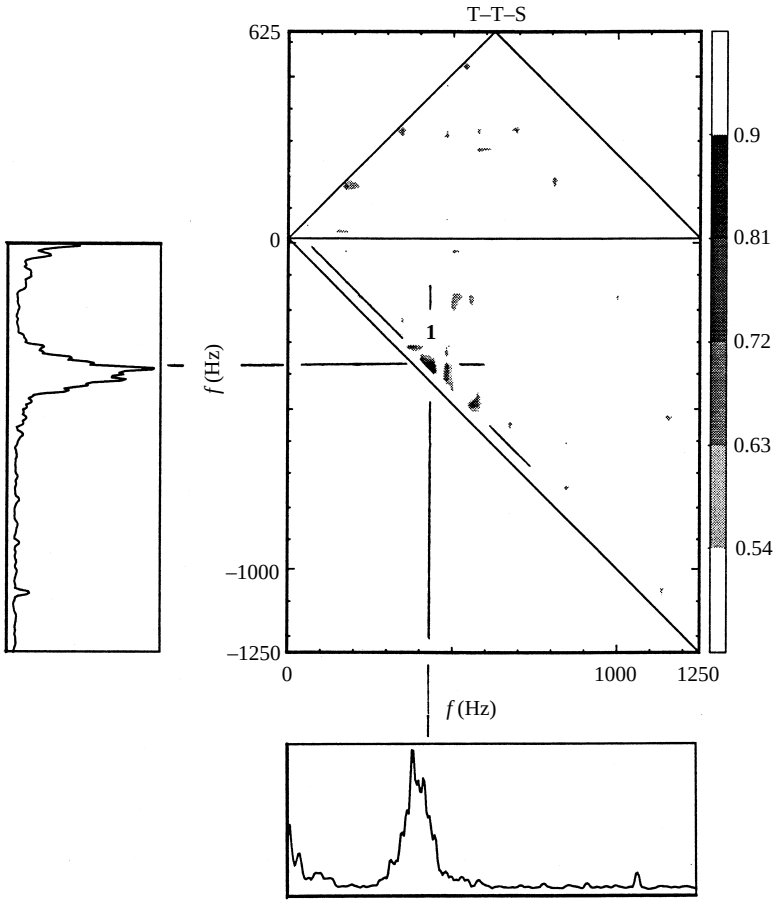

FIGURE 21. Cross-bicoherence for travelling–travelling–stationary mode interaction for the 27-dot case at $r/r_c = 1.270$ and $z^* = 1$.

although overall, the largest amplitude modes are travelling. It is therefore probable that the direction of energy transfer is still from the travelling modes into $n = 3$.

We find a similar pattern of triple phase locking between travelling and stationary modes in the the 27-dot case. This is shown in the cbc plots of figures 21 and 22. Figure 21 shows the cbc at a radius which is slightly outboard of the dots ($r/r_c = 1.27$). This is still upstream of the location of the nonlinear mean flow distortion (figure 4). Here we observe significant cbc levels for interactions between modes having the two largest peaks in the spectrum of travelling disturbances, and a stationary mode at $n = 2$ (peak 1). Phase locking between other sideband travelling modes and the $n = 2$ mode is also evident.

The number of frequencies involving interactions with the $n = 2$ mode continues to expand at further outboard radii. An example of this is shown in figure 22 which corresponds to $r/r_c = 1.585$, which is fully in the nonlinear range. As the flow progresses outward, the band of amplified frequencies shifts towards higher values. We still observe the frequency interaction corresponding to peak 1 in the previous figure (labelled peak 1 here as well); however one of the frequencies involved is now at a relatively low amplitude.

As with the 19-spiral case, in the nonlinear region we also observe interactions

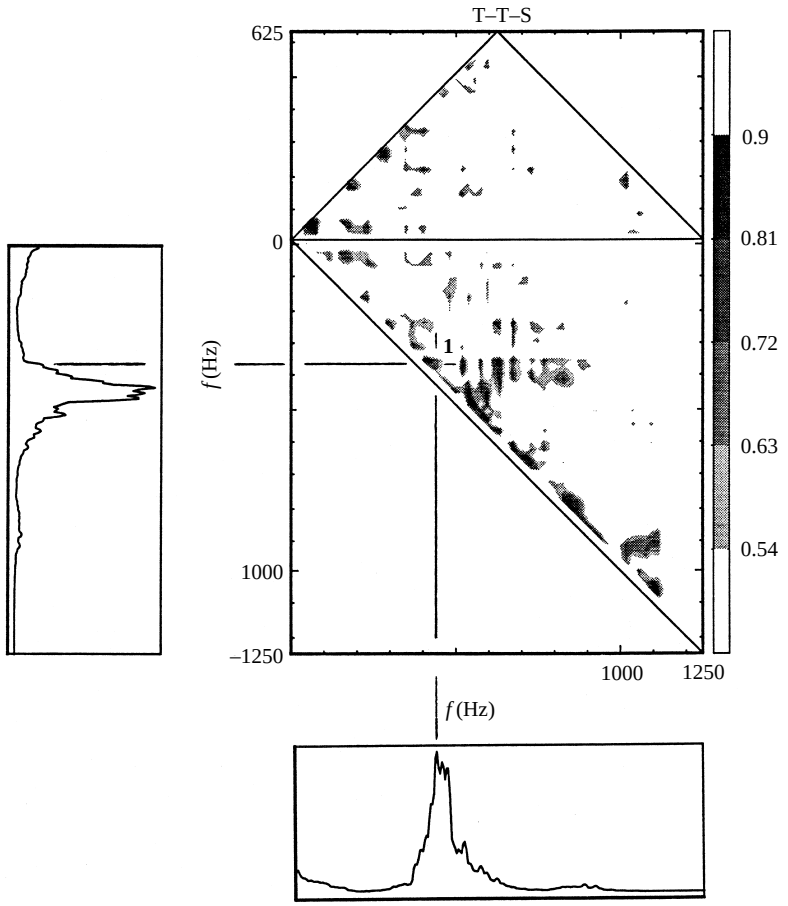

FIGURE 22. As figure 21 but at $r/r_c = 1.585$.

involving higher-mode-number stationary modes. However, as before, these involve low-amplitude travelling modes so that the dominant stationary mode at transition is at $n = 2$.

Finally, we want to demonstrate that this mechanism is not special to our dot cases, but occurs in the 'clean' case as well. Figure 23 shows the cbc for the clean/kapton disk at the most outboard radius of $r/r_c = 1.7$. In this case, the nonlinear effects occurred at a larger radius compared to the dot cases, and the flow never became turbulent on the disk. However, we observe signs of the interactions leading to the growth of a low-wave-number stationary mode in this case as well. With the 'clean' case, the interactions involve $n = 4$. The predominant interaction, involving the largest-amplitude stationary modes, is labelled peak 1. There are also other interactions with $n = 4$ that involve sideband frequencies of travelling disturbances. In addition there is significant phase locking with higher-mode-number stationary modes such as at $n = 24$ and 27. This again can account for the multi-peaked appearance of the stationary mode spectrum that we observe in the nonlinear regime in this case. If this disk had a larger radius so that we could capture transition to turbulence, we expect the development to be dominated by the low-mode-number stationary mode, in a manner which is similar to the dot cases.

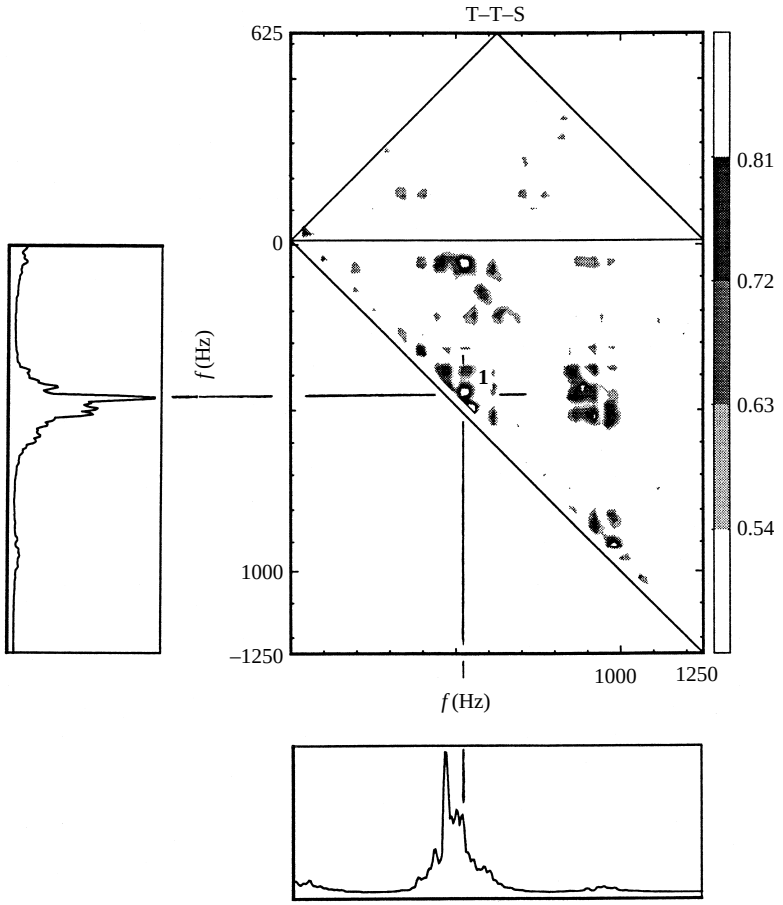

FIGURE 23. Cross-bicoherence for travelling–travelling–stationary mode interaction for clean/kapton case at $r/r_c = 1.700$ and $z^* = 1$.

4. Discussion and conclusions

The principal objective in this work was to understand better the role of travelling cross-flow modes in the process of transition to turbulence. The prevailing picture was that the action of *stationary* cross-flow vortices formed in the nonlinear region would generate an inflectional mean velocity profile which would be inviscidly unstable and break down. This scenario was graphically illustrated in flow visualization on rotating disks such as by Kobayashi *et al.* (1980) and Kohama (1984, 1987). Even though the travelling modes have higher linear growth rates, a majority of past experiments had shown the stationary modes to be dominant at transition, an effect attributed to the sensitivity of this instability to minute surface roughness. The one experiment that suggested that travelling modes were important came from Müller & Bippes (1988), which showed a reduction in the transition Reynolds number when travelling and stationary modes existed together, and achieved comparable saturation amplitudes. The larger-amplitude travelling modes in their experiment were correlated with higher free-stream disturbance amplitudes. Part of our motivation in using the roughness dots, especially in conditions like the 27-dot case, was to produce a higher-disturbance environment which would excite travelling modes.

Of course we expected the periodic roughness dots to also excite stationary modes. In this they were quite successful, and gave very repeatable results. The 19-spiral case was designed to be an ideal 'natural' case in that the azimuthal number and spiral angle were set to be the theoretically most amplified at the radius where the dots were applied. This produced the anticipated result of exciting the most-amplified azimuthal wavenumber throughout the linear regime. In contrast, the clean/kapton case represented an uncontrolled natural case. It gave an azimuthal wavenumber which was close to the most amplified, and translated into a wave angle of 12.35°, which is in the middle of the 11°–14° range generally cited in the literature. Our use of the patterned roughness was designed to overcome this variability.

The 27-dot case was designed to excite an azimuthal mode number which was not the most amplified. The dots were applied at a radius which was approximately at the middle of the linear region. Therefore we imagined that the exited $n = 27$ mode would compete with the other established and growing linear modes. We thought that the unsteadiness produced by this competition would also excite travelling modes, especially since they could more easily accommodate a different azimuthal mode number through phase speed adjustments. The stationary modes on the other hand, were found to accommodate the 27-dots by changing the azimuthal wavenumber to a less-amplified value at a significantly smaller spiral angle of 6.7°. This effect has been repeated on three occasions in two different facilities with the same results (Corke & Knasiak 1994; Knasiak 1996; Matlis 1997).

Our intention was that the roughness would be able to set the initial conditions of the cross-flow modes without having an immediate effect on the basic flow. This was confirmed in mean velocity profiles which were found to agree extremely well with the theoretical laminar profile for an infinite-radius disk. A second check was on the radial development of the boundary layer displacement thickness. In agreement with theory, we found a constant boundary layer thickness over the disk, which extended well past the location of the dots. The boundary layer thickness ultimately deviated from the constant value when the cross-flow mode amplitudes reached a sufficient level to lead to a mean flow distortion. The location of the beginning of the nonlinear distortion of the mean flow coincided well with the location of amplitude saturation of the linearly growing cross-flow modes.

In all cases we found that the development of the stationary and travelling cross-flow modes compared well with linear theory predictions. This included the linear amplification rates and wall-normal eigenfunctions. In the nonlinear region, the wall-normal amplitude distributions took on a characteristic two-peaked shape which was qualitatively similar to results from computations, such as Joslin & Streett (1994).

A guiding precept in the linear regime was that the azimuthal mode number of stationary cross-flow modes, n, would vary according to $n = \beta R$. In all the cases, this proved to be true based on time series 'peak' counts and spectra. Within the linear regime, the value of n given by the peak count corresponded to the largest-amplitude mode in the spectrum. At any radius, the spectral peak was also relatively broad and smooth, reflecting a band of growing and decaying modes which we expect from linear theory. This changed at the onset of the nonlinear regime. Here the mode predicted by $n = \beta R$ was not necessarily that with the largest amplitude. Secondly, the spectra took on a multi-peaked character, along with the emergence of a low-wavenumber stationary mode. This was true in all the cases without or with roughness dots, although the mode number varied from $n = 2$ for the 27-dot case, $n = 3$ for the 19-spiral case, and $n = 4$ for the clean/kapton case.

Following the streamwise development of the low-wavenumber stationary mode

showed that it grew only in the nonlinear region. From the onset of its growth, its wall-normal amplitude distribution was two-peaked. From these two characteristics, we deduced that it was a nonlinear mode.

Presuming that this low-number stationary mode was a nonlinear mode, we surmised that it might have originated from a triad resonance with travelling modes. Such interactions between stationary and travelling cross-flow modes have been predicted theoretically and explored in numerical simulations, but have never been documented in experiments. To test this, we examined if there was a triple phase locking between pairs of travelling modes and the low-number stationary mode. This was done by calculating the cross-bicoherence between time series which had been decomposed into stationary and travelling types. The results indicated that there was significant phase locking. This occurred through difference interactions, at first involving the largest-amplitude travelling mode, and a sideband mode. Because the amplitudes of the travelling modes were larger than the stationary mode, and the stationary mode was only found to grow in the nonlinear region, we expect that energy would be transferred from the travelling modes to the stationary mode.

With increasing Reynolds number, the number of travelling modes which were in resonance with the stationary mode increased. This is due in part to the natural shift in the most-amplified band to higher frequencies with increasing radii (Reynolds numbers). Well into the nonlinear region, other interactions which involved higher-mode-number stationary modes were found to occur. These accounted for the multi-peaked character that the stationary mode spectrum developed in the nonlinear region.

The triple phase locking is one of the two conditions necessary to confirm resonance. The other is wavenumber matching between the three modes. For the travelling modes, this involves simultaneously sampling two velocity time series at two spatial locations, in two configurations, to resolve the two-dimensional wavenumber vector, $k_i = (\alpha_i^2 + \beta_i^2)^{1/2}$, where i refers to the index of one of the interacting frequencies. The second condition for resonance is that $k_1 \pm k_2 = k_3$. This confirming step has been performed by Matlis (1997) and is described by Corke & Matlis (1997).

One of the open questions is what determined the dominant low mode number, which was different in the three cases. Since they appeared to originate from the travelling modes, we suppose that the selection was based on differences in the spectrum of travelling disturbances. The two dot cases were intrinsically different, with the principal function of controlling the conditions of stationary modes. The past experiments of Wilkinson & Malik (1985) and Blanchard (1992), with a single isolated bump, indicated that such roughness produces wave packets which travel around the disk. The spectra of the travelling modes indicated that our periodic roughness initially excited a narrow frequency band at values that were consistent with the dot mode number and the fact that theory predicts that their phase velocity should not be far from the disk speed. In all the cases, the spectra of the travelling modes quickly developed a multi-peaked character. The cross-bicoherence indicated that these frequencies were involved in the resonance process with the low-number stationary mode in each case. Recent measurements by Matlis (1997) however indicate that the selection process is not precisely repeatable. In his re-creation of the 19-spiral and 27-dot cases, he found that the low-number azimuthal modes which were dominant at transition were at $n = 4$ and 5, respectively. The physics of the process was found to be the same in that he verified both frequency and wavenumber matching between the pairs of travelling mode and the low-number stationary mode. It was only that the mode number in his cases was slightly different.

Although the low-number stationary mode did not reach quite as high an amplitude as the largest-amplitude travelling modes, at transition it was the largest-amplitude stationary mode. As such, it had a significant impact on the mean flow. This was seen as a low-wavenumber variation of the boundary layer thickness which emerged at the end of the nonlinear region.

Can we find evidence of this mechanism in other experiments? There are no comparable quantitative measurements that we are aware of; however we believe that we can find evidence in some of the earlier flow visualization records of rotating disk flows. For example, those of Kobayashi *et al.* (1980, and reproduced in figure 132 of Van Dyke 1981), which have been frequently cited to demonstrate the high-frequency inviscid transition mechanism, clearly show a large wavelength, $n = 3$, variation in the smoke density at transition. Others by Kohama (1984, figure 2*b* and 1987, figure 1(b, c)) show a similar variation with slightly different mode numbers. Also, a general characteristic of the cross-flow instability on a swept wing is the appearance of a long-wavelength (many times the cross-flow spacing) 'jagged' transition front. We would obtain a similar picture in our experiment if we were to unwrap the disk flow into Cartesian coordinates. Although this is not a proof that the same mechanism is involved, it could account for this appearance and suggest an important role of the travelling modes in transition to turbulence in this flow.

We gratefully acknowledge the supported from NASA Langley Research Center, and Steve Wilkinson who was the scientific monitor.

REFERENCES

Arnal, D. & Juillen, J. 1987 Three-dimensional transition studies at ONERA/CERT. *AIAA Paper* 87-1335.

Bippes, H. 1991 Experiments on transition in three-dimensional accelerated boundary layer flow. In *R. Aeronaut. Soc. Conf. on Boundary Layer Transition & Control, Cambridge, UK*.

Blanchard, A. E. 1992 Experimental investigation of cross-flow instability waves in rotating disk flow. MS Thesis, Old Dominion University.

Corke, T. & Knasiak, K. 1994 Cross-flow instability with periodic distributed roughness. In *Transition, Turbulence & Combustion*, Vol. I, p. 43. Kluwer.

Corke, T. & Matlis, E. 1997 Wave number analysis and resonance of stationary and travelling cross-flow modes on a rotating disk. To be submitted to *J. Fluid Mech.*

Corke, T. C., Shakib, F. & Nagib, H. 1991 Mode selection and resonant phase locking in unstable jets. *J. Fluid Mech.* **223**, 253.

Dagenhart, J., Saric, W., Mousseux, M. & Stack, J. 1989 Crossflow-vortex instability and transition on a 45-degree swept wing. *AIAA Paper* 89-1892.

Faller, A. J. 1991 Instability and transition of disturbed flow over a rotating disk. *J. Fluid Mech.* **230**, 245.

Federov, B., Plavnik, G., Prokhorov, I. & Zhukhovitskii, L. 1976 Transitional flow conditions on a rotating disk. *J. Engng Phys.* **31**, 1448.

Gregory, N., Stuart, J. & Walker, W. 1955 On the stability of three-dimensional boundary layers with applications to the flow due to a rotating disk. *Phil. Trans. R. Soc. Lond.* A **248**, 155.

Jarre, S., Le Gal, P. & Chauve, M. 1996 Experimental study of disk flow instability. II. Forced flow. *Phys. Fluids* **8**, 2985.

Joslin, R. D. & Streett, C. L. 1994 The role of stationary cross-flow vortices in boundary-layer transition on swept wings. *Phys. Fluids* **6**, 3442.

Knasiak, K. 1996 Stability of rotating disk flow with distributed surface roughness: linear and nonlinear development. MS Thesis, Illinois Institute of Technology.

Kobayashi, R., Kohama, Y. & Takamadate, Ch. 1980 Spiral vortices in boundary layer transition regime on a rotating disk. *Acta Mech.* **71**, 71.

Kohama, Y. 1984 Study on boundary layer transition of a rotating disk. *Acta Mech.* **50**, 193.

KOHAMA, Y. 1987 Cross-flow instability in rotating disk boundary-layer. *AIAA Paper* 87-1340.

KOHAMA, Y., SARIC, W. S. & HOOS, J. A. 1991 A high frequency secondary instability of cross flow vortices that leads to transition. In *Boundary Layer Transition and Control*, p. 4.1. Royal Aero. Soc., London, UK.

LEKOUDIS, S. 1979 Resonant wave interactions on a swept wing. *AIAA J.* **18**, 122.

MACK, L. M. 1985 The wave pattern produced by a point source on a rotating disk. *AIAA Paper* 85-0490.

MALIK, M. 1986 The neutral curve for stationary disturbances in rotating disk flow. *J. Fluid Mech.* **164**, 275.

MALIK, M., LI, F. & CHANG, C-L. 1994 Crossflow disturbances in three-dimensional boundary layers: nonlinear development, wave interaction and secondary instability. *J. Fluid Mech.* **268**, 1.

MALIK, M., WILKINSON, S. & ORSZAG, S. 1981 Instability and transition in rotating disk flow. *AIAA J.* **19**, 1131.

MATLIS, E. 1997 Wave number analysis and resonance of stationary and travelling cross-flow modes on a rotating disk. MS Thesis, Illinois Institute of Technology.

MÜLLER, B., BESTEK, H. & FASEL, H. 1995 Nonlinear development of travelling waves in a three-dimensional boundary layer. In *Nonlinear Stability and Transition in Three Dimensional Boundary Layers*. Kluwer.

MÜLLER, B. & BIPPES, H. 1988 Experimental study of instability modes in a three-dimensional boundary layer. *AGARD-CP*-438, No. 18.

POLL, I. 1985 Some observations of the transition process on the windward face of a long yawed cylinder. *J. Fluid Mech.* **150**, 329.

RADEZTSKY, R., RIEBERT, M., SARIC, W. & TAKAGI, S. 1993 Effect of micron-sized roughness on transition in swept-wing flows. *AIAA Paper* 93-0076.

REED, H. L. & SARIC, W. S. 1989. Stability of three dimensional boundary layers. *Ann. Rev. Fluid Mech.* **21**, 235.

SMITH, N. 1946 Exploratory investigation of laminar boundary layer oscillations on a rotating disk. *NACA TN* 1227.

SPALART, P. R., 1991 On the cross-flow instability near a rotating disk. *Proc. R. Aeronat. Soc. Boundary Layer Transition and Control, Cambridge, UK*, pp. 22.1.

VAN DYKE, M. (ED.) 1981 *An Album of Fluid Motion.* Parabolic Press, Stanford, CA.

WILKINSON, S. & MALIK, M. 1985 Stability experiments in the flow over a rotating disk. *AIAA J.* **23**, 588.